Science Advances

AAAS

advances.sciencemag.org/cgi/content/full/3/5/e1602371/DC1

Supplementary Materials for

Low-energy structural dynamics of ferroelectric domain walls in hexagonal rare-earth manganites

Xiaoyu Wu, Urko Petralanda, Lu Zheng, Yuan Ren, Rongwei Hu, Sang-Wook Cheong, Sergey Artyukhin, Keji Lai

Published 10 May 2017, *Sci. Adv.* **3**, e1602371 (2017)
DOI: 10.1126/sciadv.1602371

This PDF file includes:

section S1. dc conductivity of h-*R*MnO_3

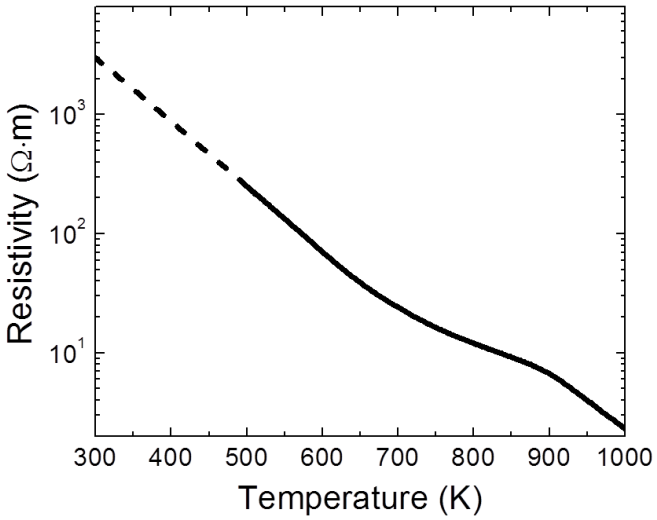

fig. S1. Measurement of the dc resistivity of $YMnO_3$.

The dc resistivity of our single-crystal $YMnO_3$ samples is measured by a four-probe method using a Keithley source meter. The electrical contacts are made by curing the gold paste at high temperatures between 600 K and 800 K. The results from 1000 K to 500 K are shown in a solid curve because good Ohmic contacts are achieved in this temperature range. The kink at ~ 850 K is likely due to the formation of oxygen interstitials, which effectively dope the surface of the crystals (*28*). For temperatures below 500 K, the contact resistance becomes substantially large and the I-V curves are no longer Ohmic-like. An extrapolation from ~ 600 K to ~ 300 K indicates a room-temperature dc resistivity of ~ 3×10^3 Ω·m, or the conductivity of ~ 0.3×10^{-3} S/m, which is consistent with the number (on the order of 10^{-3} S/m) quoted in the literature (*31*, *33*, *34*). Future experiments using samples with improved Ohmic contacts and instruments with higher input impedance may provide a more quantitative room-temperature dc resistivity of the $YMnO_3$ crystals.

section S2. SIM electronics and the calibration process

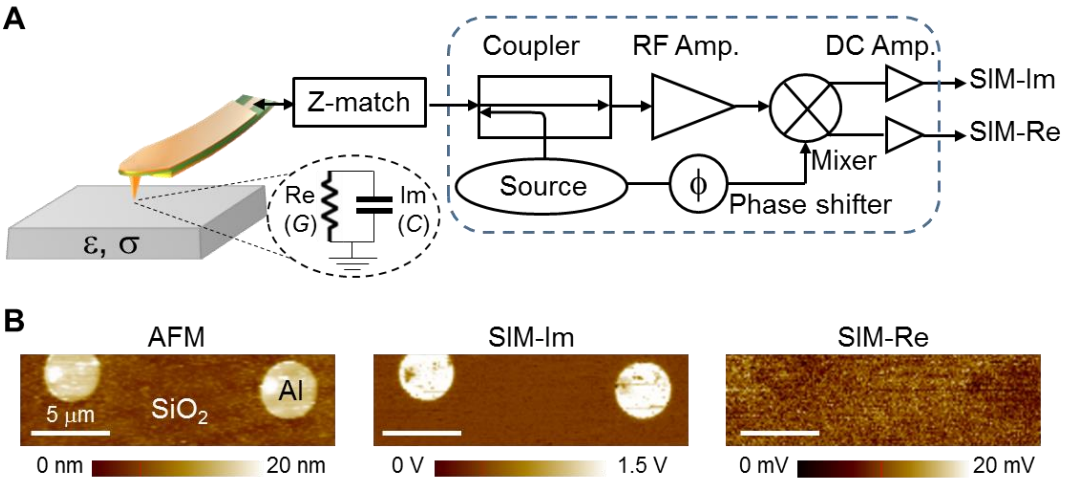

fig. S2. SIM electronics and the calibration process. (**A**) Schematics of the SIM electronics. (**B**) AFM and SIM images (f = 1 GHz) on the standard sample with Al dots on the SiO_2/Si substrate. All scale bars are 5 μm.

The schematic diagram of the SIM electronics is shown in fig. S2A. The radio-frequency (rf) signal is sent to the tip through an impedance-match section, which is a quarter-wave resonator with a small reflection coefficient (S_{11} ~ -20 dB) at f = 1 GHz. All our measurements are performed in the linear regime, i.e., the SIM output is proportional to the tip voltage. With a typical excitation power of 10 μW, a simple transmission-line analysis taking into account the cable loss show that the rf voltage at the tip is on the order of 0.1 V. The reflected wave is amplified and demodulated to form the two output channels. The SIM-Re and SIM-Im signals are proportional to the real (in-phase) and imaginary (out-of-phase) parts of the tip-sample admittance, respectively.

An important step before the actual measurement is the channel alignment using standard samples such as Al dots on the SiO_2/n++Si substrate. On this sample, the tip-sample capacitance is different between the ~4 nm native Al_2O_3 (on top of the metallic Al) and the 100 nm SiO_2 (on top of the metallic n++ Si). As a result, the contrast should appear only in the SIM-Im channel. This condition is met by adjusting the phase shifter in front of the mixer to nullify the contrast in the SIM-Re channel. As shown in fig. S2B, we can obtain good channel alignment at 1 GHz, with a residual SIM-Re/Im ratio < 1%. Even towards the frequency limits of our broadband SIM (1 MHz and 10 GHz), an uncertainty within 5% is feasible. Since the SIM-Re/Im data points in Fig. 3 are all larger than 0.05, the results are genuine effects rather than instrumental artifacts.

section S3. FEA of the tip-sample interaction

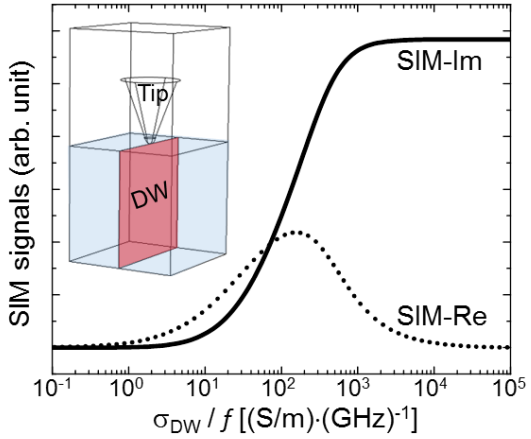

fig. S3. FEA of the tip-sample interaction. Finite-element analysis (FEA) of the SIM signals as a function of σ_{DW}, which is scaled by the frequency in unit of GHz. The 3D modeling geometry is shown in the inset.

The FEA results are shown in fig. S3. Here SIM-Re and SIM-Im signals are directly proportional to the real and imaginary parts of the tip-sample admittance (inverse impedance), which can be computed by the software COMSOL 4.4 (*36*). Note that the SIM signals saturate at both the low (below 1 S/m at 1 GHz) and high (above 10^4 S/m at 1 GHz) conductivity limits. Due to the small bulk conductivity $\sigma_{bulk} \sim 10^{-3}$ S/m, the SIM response on the bulk domains is in the insulating limit. The quasi-static simulation is invariant when the effective DW conductivity σ_{DW} is scaled by the frequency, i.e., the curves shift to higher σ_{DW} at higher frequency and vice versa. A tip diameter (d) of 100 nm was used in the modeling, consistent with the SEM image at the tip apex and the line profiles in Fig. 1C. The domain wall width (λ) on the order of 1 nm was reported in previous transmission electron microscopy studies (*37, 52*). We assign λ = 2 nm so that it is easy to generate a dense mesh in the simulation. In fact, since $d >> \lambda$, the modeling result is invariant with respect to the effective sheet conductance $S_{DW} = \sigma_{DW} \cdot \lambda$. For instance, σ_{DW} = 500 S/m and λ = 2 nm lead to S_{DW} = 1 μS·sq and an effective sheet resistance $R_{DW} = 1/S_{DW}$ = 1 MΩ/sq. Due to the relatively small static dielectric constant ε_s = 17 of the improper ferroelectric h-*R*MnO_3 (*53*), it is unlikely that a possible dipolar relaxation process (*54*) (ε' drops from ε_s to $\varepsilon_\infty < \varepsilon_s$ and ε'' peaks at $(\varepsilon_s + \varepsilon_\infty)/2$) within our frequency span will substantially affect the simulation result. As a result, we have chosen to interpret the observed impedance contrast in terms of a single parameter, i.e., the effective ac conductivity of the DWs, while making the reasonable assumption of *f*-independent dielectric constant ε = 17 for both domains and DWs.

section S4. SIM data on polished $HoMnO_3$ samples

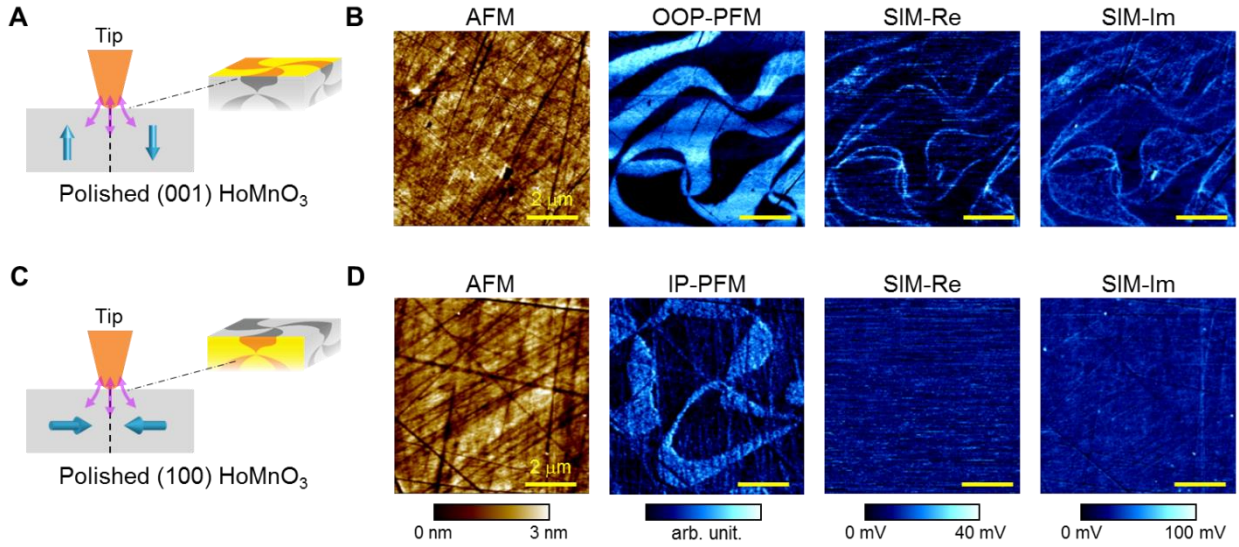

fig. S4. SIM data on polished $HoMnO_3$ samples. (**A**) Schematic and (**B**) AFM, out-of-plane PFM, and SIM images on the polished (001) surface of $HoMnO_3$ single crystal. (**C**) Schematic and (**D**) AFM, in-plane PFM, and SIM images on polished (100) surface cut from the same sample. All scale bars are 1 μm.

In addition to the as-grown $YMnO_3$, $ErMnO_3$ and cleaved $HoMnO_3$ samples presented in the main text, we have also measured other samples to confirm that the results are common to the h-$RMnO_3$ family. In particular, we cut and polished two samples, one with (001) surface and the other with (100) surface, from one single piece of $HoMnO_3$. Note that the SIM data are usually of low quality for polished samples with inevitable scratches and possible damages on the surface. Nevertheless, the images in fig. S4, B and D clearly show the appearance and absence of DW contrast on the (001) and (100) surfaces, respectively. In addition, the SIM-Re/Im ratio of the (001) sample (0.40±0.10) is consistent with that on the $YMnO_3$ and $ErMnO_3$ samples. We therefore conclude that the observed DW signals do not depend on the choice of the rare-earth element *R*, and the DW contrast is most prominent on the *ab*-plane with out-of-plane polarizations (*31*) and absent on surfaces parallel to the *c*-axis with in-plane polarizations (*42*, *43*).

section S5. SIM circuits and impedance match at different frequencies

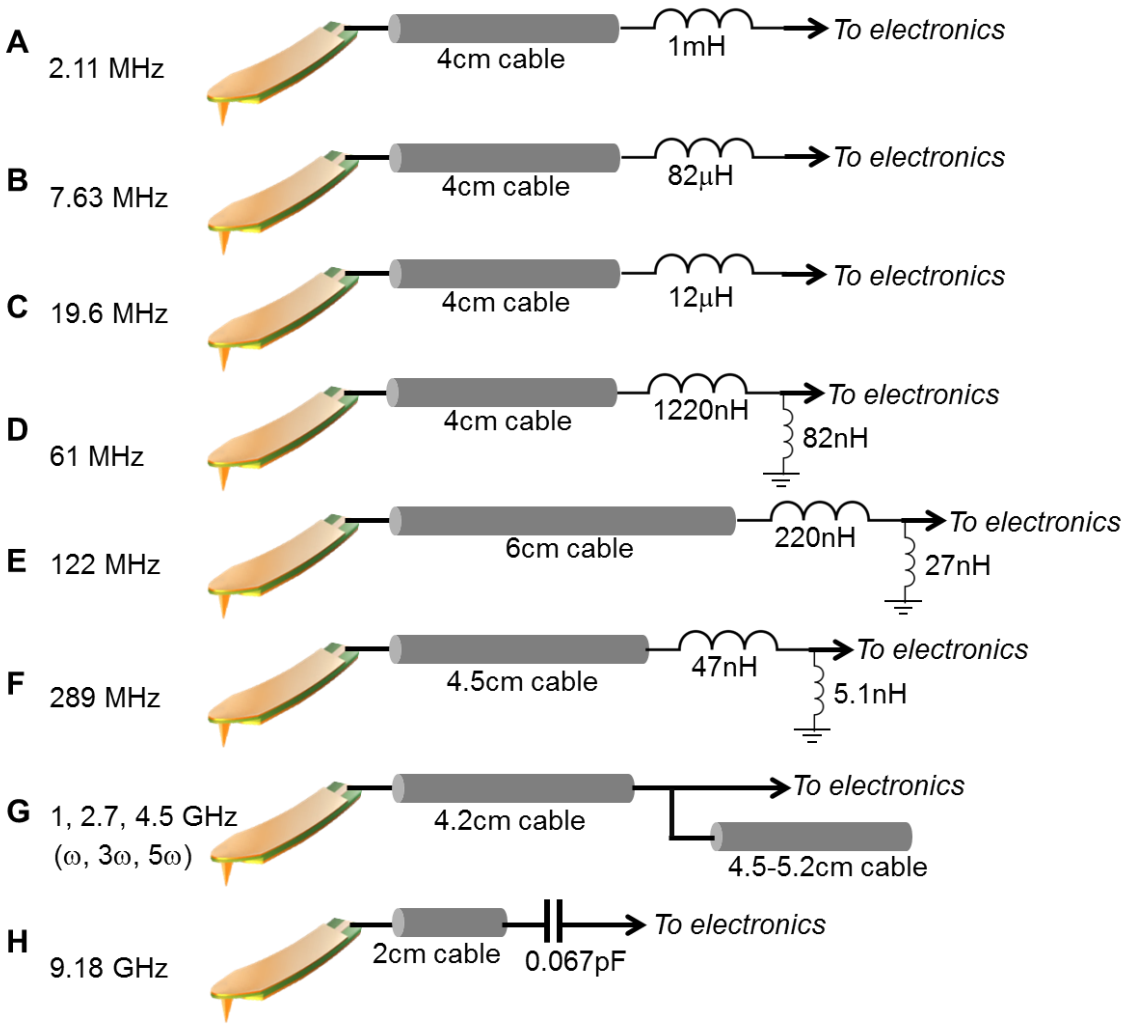

fig. S5. Impedance-match sections at different frequencies. (**A-H**) Impedance-match sections for all frequency points in this experiment.

We have constructed three sets of SIM electronics to obtain the best sensitivity around 100 MHz, 1 GHz, and 10 GHz, respectively. For frequencies below 50 MHz, we configured the HF2LI lock-in amplifier from Zurich Instruments to perform the SIM imaging. In addition, an impedance-match section (*36*) is needed at each frequency to route the tip to the 50 Ω transmission lines, as shown in fig. S5. The impedance match is important to enhance the measurement sensitivity. It also adds another complication when comparing the absolute signal strengths at different frequencies. Again, the aforementioned method of taking the SIM-Re/Im ratio effectively cancels out this circuit-dependent factor and is therefore preferred for quantitative analysis of the DW signals.

section S6. More SIM data at various frequencies

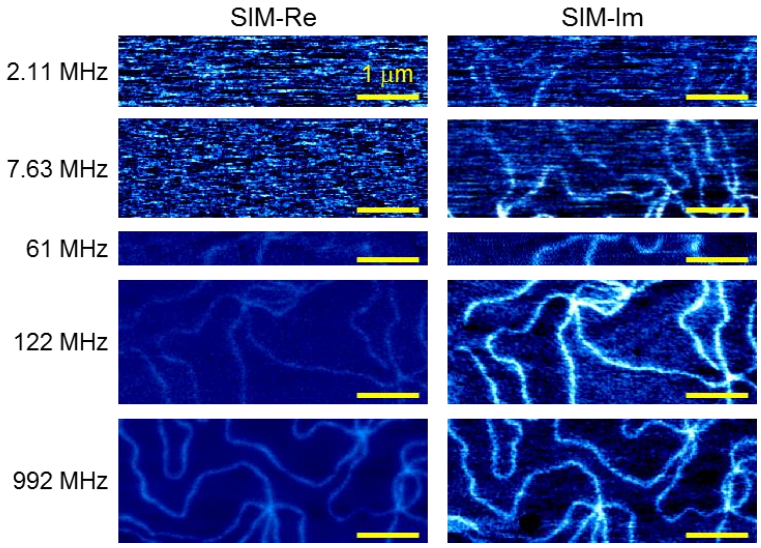

fig. S6. SIM images at various frequencies. All scale bars are 1 μm.

SIM images not shown in the main text (Fig. 3A) are included in fig. S6. For each *f*, the SIM-Re and SIM-Im images are displayed with the same false-color scale. The absolute signals, however, cannot be compared between different electronics and therefore are not shown here.

section S7. Repeated line scans for improving the signal-to-noise ratio

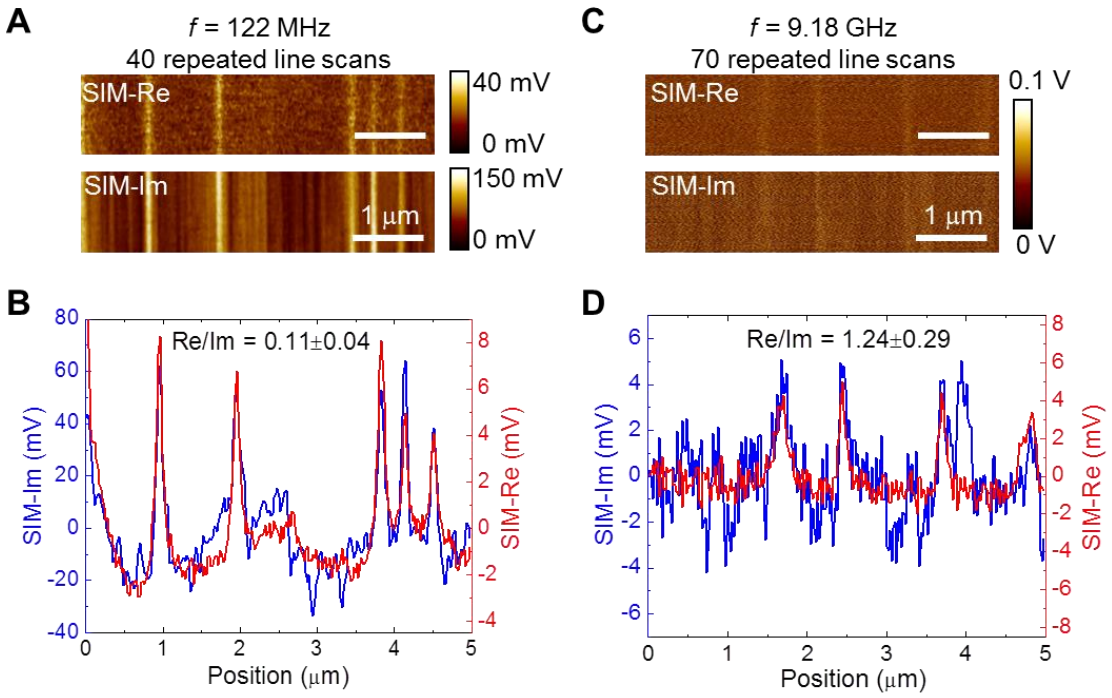

fig. S7. SIM experiments with repeated line scans. (**A**) Repeated SIM line scans at f = 122 MHz and (**B**) the corresponding averaged signals for calculating SIM-Re/Im with a better signal-to-noise ratio. (**C**) and (**D**) show the same results acquired at f = 9.18 GHz. All scale bars are 1 μm.

For the same capacitance contrast ΔC, the admittance change ($2\pi f \cdot \Delta C$) becomes smaller at lower frequencies, which is thus harder to detect by the SIM electronics. The lowest frequency in this work is ~ 2 MHz, below which the signal-to-noise ratio (SNR) is too low for the imaging experiment. At high frequencies, the loss in the coaxial cables and the shielded cantilever sets our upper limit to be ~ 10 GHz, beyond which the SNR is again too low for imaging.

To extract the SIM-Re/Im ratio of the DW contrast, we perform repeated line scans to improve the SNR of the data. Figure S7, A and B show the results (f = 122 MHz) of 40 scans on the same line and the plot of averaged SIM signals, respectively. For the f = 9.18 GHz data shown in fig. S7, C and D, the DWs are hardly seen in the raw data due to the poor sensitivity. The line averaging method, however, provides adequate SNR such that the SIM-Re/Im ratio can be readily calculated.

section S8. Details of the full model calculations

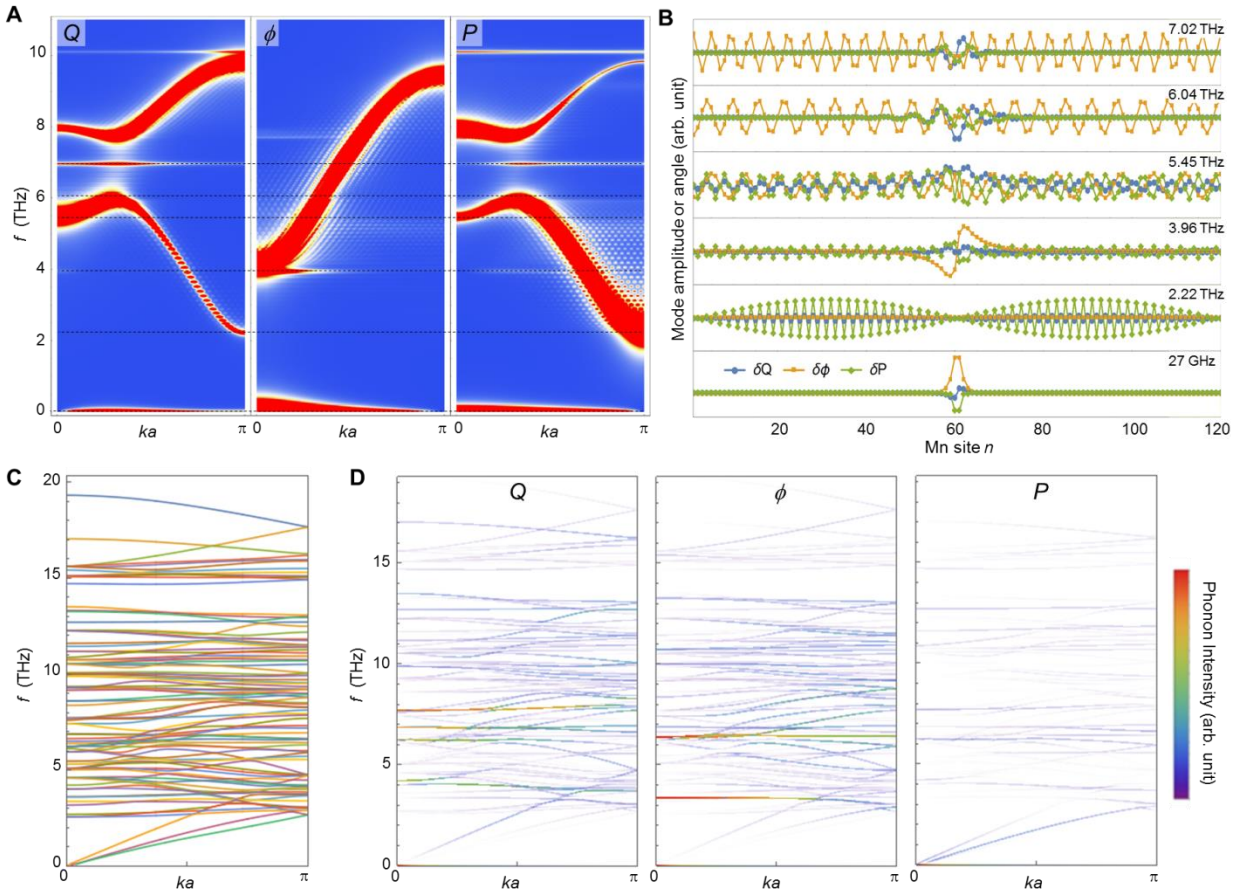

fig. S8. First principles–based model calculations. (**A**) Phonon spectral function displayed in Fig. 5C. (**B**) Oscillation amplitudes of the local modes Q, ϕ, and P are shown for several characteristic phonons at frequencies labeled in **A** with the dashed lines. (**C**) Phonon dispersion of $YMnO_3$ in the low temperature $P6_3cm$ structure. (**D**) From left to right: Contributions of the Q, ϕ, and P modes to the phonon dispersion. The lines are color coded with the relative intensity.

In improper ferroelectric $YMnO_3$ the trimerization and polarization are strongly coupled, therefore the structural (trimerization) antiphase boundaries are also ferroelectric DWs. In order to get a quantitative estimate for the sliding mode frequency, we extend the model to incorporate the principal modes, Q, ϕ and P, appearing at the trimerization transition. The structural changes across the domain walls and other non-uniform trimerization textures are primarily described by the modulation of these modes (*44*). We therefore use the discretized version of the model (*44*), involving all the relevant degrees of freedom, Q, ϕ, and P, and replace the gradient terms with

the corresponding interactions between the neighboring sites

$$H = \sum_{n=1}^{L} \frac{\left(\dot{Q}_n\right)^2 + Q_n^2 \dot{\phi}_n^2}{2m_Q} + \frac{\left(\dot{P}_n\right)^2}{2m_P} - A_1\left(Q_n^2 - Q_0^2\right)^2$$
$$-c_1\left(\left(Q_n - Q_{n+1}\right)^2 + \frac{\left(Q_n + Q_{n+1}\right)^2\left(\phi_n - \phi_{n+1}\right)^2}{4}\right) \qquad [S1]$$
$$-A_2 P_n^2 - c_2\left(P_n - P_{n+1}\right)^2 - g_1 Q_n^3 P_n \cos 3\phi_n - g_2 Q_n^2 P_n^2$$

In order to approximate the realistic phonon dispersion, we use the corresponding interaction constants and mode masses to fit the phonon band dispersion and band center positions to those determined by the DFT calculations. To calculate the phonons within the model, the Hamiltonian is expanded around the equilibrium DW configuration, up to the terms, quadratic in deviations from the ground state DW, and the corresponding Euler-Lagrange equations are solved as an eigenvalue problem. The finite chain is used with the fixed boundary conditions. The resulting phonon modes with energies E_n and amplitudes $x_{nm}^{(\alpha)}$ of the mode α (α = 1, 2, 3 for modes Q, ϕ, and P) on the site m can be visualized by plotting the phonon spectral function in fig. S8A

$$A_{\alpha\beta}(k,\omega) = \sum_n \delta(\omega - E_n)\left\langle k \middle| x_{nm}^{(\alpha)} \right\rangle \left\langle x_{nm}^{(\beta)} \middle| k \right\rangle \qquad [S2]$$

Here the summation runs over all phonon branches n, $|\mathrm{k}\rangle = \mathrm{e}^{\mathrm{i\,k\,m}}$ is a plane wave with the wave vector k. A scalar product is defined in the usual way, $\langle \mathrm{k}|\mathrm{x_{nm}}\rangle = \sum_{\mathrm{m}} \mathrm{e}^{-\mathrm{i\,k\,m}}\mathrm{x_{nm}}$. And we use a finite-width approximation to a δ-function to describe a finite lifetime. The result looks similar to the phonon dispersion of a periodic crystal, but the translation symmetry breaking due to the DW is manifested in the normal modes at a given frequency not having a single plane wave form with fixed k, but instead a combination of plane waves with different wave vectors.

The spectral function projected on the oscillations of Q, ϕ, and P modes resembles the bulk phonon dispersion with the dispersive branches for Γ_2^- and K_3 phonons, along with several non-dispersive branches, corresponding to the phonons localized at the DWs. Here a damping parameter of 20 GHz, consistent with the optical experiments (*49*), is used in the calculations. The ripples in the false-color maps (fig. S8A) are due to the finite size of the supercell. fig. S8B shows the real-space oscillation of δQ, $\delta\phi$, and δP at several characteristic frequencies. The lowest branch, appearing in the GHz range, corresponds to the oscillations of the DW position

around the equilibrium position, while the localized modes at the THz range correspond to the width oscillations of the Q, ϕ, and P textures. Note that DW-sliding mode is localized only perpendicular to the DW plane and free to propagate within the DWs. Our 1D calculation, therefore, only shows the bottom of the phonon band. The sliding mode with non-zero k_y, k_z wave vectors in the DW plane are analogous to the acoustic waves in elastic media. The inter-site mode coupling terms similar to those with c_1, c_2 in Equation [S1] give rise to the phonon dispersion for the wave vector components in the DW plane (e.g. yz). These terms give rise to the band of DW-localized phonons, with phonon amplitudes in the DW plane having the oscillating form $\exp(k_y y+k_z z)$, and the bandwidth determined by the respective stiffness constants, and therefore of the same order as the bandwidth of Γ_2^- and K_3 bands in the bulk.

The phonon calculations are performed using frozen-phonon method as implemented in Phonopy software, within the 3×3×2 supercell of the $P6_3cm$ low-temperature unit cell using generalized gradient approximation to density functional theory (GGA, DFT) with a plane wave basis set and projector-augmented waves formalism as implemented in the Quantum Espresso package (*55, 56*). The plane wave cut-off of 35 Ry and density cut-off of 300 Ry are used. The magnetic ordering is approximated by A-type antiferromagnetism, which should be sufficient for the present estimates and LDA+U with atomic projection and U = 4 eV was used (*57*). The results of the phonon dispersion (fig. S8C) and contributions from the Q, ϕ, and P modes are shown in fig. S8D. The discrete model is then constructed using the force constants calculated, with the energy of the domain wall minimized in the harmonic approximation, which is justified by the small tilts of bi-pyramids from the equilibrium positions in the two domains. Then the energy is expanded around this state and the phonons are calculated. The results, projected on the phase and amplitude modes of trimerization and on polarization are shown in fig. S8A.

This approach, combining models and first-principles calculations, allows us to treat the bulk and DW-specific phonons within the unified picture and clarifies the physics of the localized low-energy excitation in the SIM data.